HHS Public Access

Author manuscript

Neuroimage. Author manuscript; available in PMC 2016 May 15.

Published in final edited form as:

Neuroimage. 2015 May 15; 112: 43–51. doi:10.1016/j.neuroimage.2015.02.052.

Enhanced Identification of BOLD-like Components with Multi-Echo Simultaneous Multi-Slice (MESMS) fMRI and Multi-Echo ICA

Valur Olafsson[a], **Prantik Kundu**[b,c], **Eric C. Wong**[d,e,f], **Peter A. Bandettini**[g,h], and **Thomas T. Liu**[d,e,i]

[a]Neuroscience Imaging Center, University of Pittsburgh, 3025 E Carson St, Pittsburgh, PA 15203, USA

[b]Brain Imaging Center, Icahn Institute of Medicine at Mt. Sinai, 1470 Madison Ave, 1st floor, New York, NY 10029, USA

[c]Translational and Molecular Imaging Institute, Icahn Institute of Medicine at Mt. Sinai, 1470 Madison Ave, 1st floor, New York, NY 10029, USA

[d]Center for Functional Magnetic Resonance Imaging, University of California San Diego, 9500 Gilman Drive, La Jolla, CA 92093, USA

[e]Department of Radiology, University of California San Diego, 9500 Gilman Drive, La Jolla, CA 92093, USA

[f]Department of Psychiatry, University of California San Diego, 9500 Gilman Drive, La Jolla, CA 92093, USA

[g]Section on Functional Imaging Methods, National Institute of Mental Health, 6001 Executive Boulevard, Bethesda, MD, USA

[h]Functional MRI Core Facility, National Institute of Mental Health, 6001 Executive Boulevard, Bethesda, MD, USA

[i]Department of Bioengineering, University of California San Diego, 9500 Gilman Drive, La Jolla, CA 92093, USA

Abstract

The recent introduction of simultaneous multi-slice (SMS) acquisitions has enabled the acquisition of blood oxygen level dependent (BOLD) functional magnetic resonance imaging (fMRI) data

Correspondence to: Valur Olafsson, Ph.D., University of Pittsburgh, Neuroscience Imaging Center, 3025 E Carson St, Pittsburgh, PA 15203, Phone: 412 383 7108, Fax: 412 383 6799, vto77@pitt.edu; Prantik Kundu, Ph.D., Brain Imaging Center and Translational and Molecular Imaging Institute, Icahn Institute of Medicine at Mt. Sinai, 1470 Madison Ave, 1st floor, New York, NY 10029, Phone: 212-824-8465, prantik.kundu@mssm.edu; Thomas T. Liu, Ph.D., UCSD Center for Functional MRI, 9500 Gilman Drive, MC 0677, La Jolla, CA 92093-0677, Phone: 858-822-0542; Fax: 858-822-0605; ttliu@ucsd.edu.
Dual first authors: Valur Olafsson and Prantik Kundu

with significantly higher temporal sampling rates. In a parallel development, the use of multi-echo fMRI acquisitions in conjunction with a multi-echo independent component analysis (ME-ICA) approach has been introduced as a means to automatically distinguish functionally-related BOLD signal components from signal artifacts, with significant gains in sensitivity, statistical power, and specificity. In this work, we examine the gains that can be achieved with a combined approach in which data obtained with a multi-echo simultaneous multi-slice (MESMS) acquisition are analyzed with ME-ICA. We find that ME-ICA identifies significantly more BOLD-like components in the MESMS data as compared to data acquired with a conventional multi-echo single-slice acquisition. We demonstrate that the improved performance of MESMS derives from both an increase in the number of temporal samples and the enhanced ability to filter out high-frequency artifacts.

Introduction

Resting-state functional connectivity magnetic resonance imaging (fcMRI) has emerged as a widely used approach to characterize the functional connectivity of the brain at rest. The recent advent of simultaneous multi-slice (SMS) acquisitions has made it possible to routinely acquire whole-brain fcMRI datasets with temporal sampling rates that are significantly higher than those of conventional acquisitions (Moeller et al., 2010; Setsompop et al., 2012). Depending on spatial resolution, these sampling rates have ranged from 0.5 Hz and 3.0Hz (Kalcher et al., 2014). The higher sampling rate can be used to reduce temporal aliasing of high frequency noise sources, increase statistical power, and improve the characterization of the temporal and spatial features of resting-state networks (Feinberg et al., 2010; Griffanti et al., 2014; Smith et al., 2013).

In a parallel line of work, the combination of multi-echo acquisitions with an independent component analysis framework (ME-ICA) has recently been introduced as an effective method for the automatic identification and removal of physiological noise and motion artifacts from fMRI time series data, with significant gains in sensitivity, statistical power, and specificity (Kundu et al., 2013; Kundu et al., 2012; Kundu et al., 2014). In the ME-ICA approach, independent components whose amplitudes exhibit a linear dependence on echo time are designated as functionally-related blood oxygen level dependent (BOLD) components. These are distinguished from non-BOLD-like components that do not exhibit this linear dependence on echo time and largely reflect subject motion, scanner and physiological artifacts, and thermal noise contributions.

In this study, we examine the performance of a combined approach in which resting-state fMRI data are acquired with a multi-echo and simultaneous multi-slice (MESMS) acquisition. Preliminary work in this area suggests that MESMS acquisitions can improve the ability to detect and characterize resting-state networks as compared to conventional multi-echo single-slice excitation (MESS) acquisitions (Boyacioglu et al., 2013; Boyacioglu et al., 2014; Olafsson et al., 2012; Olafsson et al., 2013; Olafsson et al., 2014). Here we build upon these preliminary studies and present a systematic study of MESMS, in terms of the applicability of ME-ICA, the effect of temporal resolution, time course pre-filtering, and functional time course signal bandwidth on the ability of ME-ICA to identify BOLD-related

functional components. This involves comparing the performance of ME-ICA when applied to data from both MESMS and MESS acquisitions, and assessing the performance of ME-ICA for MESMS data after the application of a range of pre-filtering and resampling operations.

Methods

Overview

Here we describe methods of MESMS-fMRI acquisition and analysis. An overview of ME-ICA is given here, with further technical detail on decomposition and BOLD/non-BOLD component differentiation provided in the appendix, and in (Kundu et al 2013). The remaining material describes the filtering and resampling strategies employed to produce derived datasets that were then used to assess the relevance of temporal bandwidth and temporal aliasing in elucidating BOLD components.

Experimental Protocol

We collected MRI data from twelve subjects (six women, average age ± std was 28.5 ± 5.2 years) who signed informed consent forms approved by the UCSD Institutional Review Board. For each subject, two 10-minute BOLD fMRI resting state scans were collected in the same scan session. One of the resting state scans was collected with multi-echo simultaneous multi-slice (MESMS) echo-planar imaging (EPI) and the other with multi-echo single-slice (MESS) EPI. Note that while the MESS acquisition entails acquiring multiple slices across the brain volume, we have used the “single-slice” designation to indicate that only one slice is excited at a time. The order of these acquisitions was randomized across subjects, with six subjects having the MESMS scan acquired before the MESS scan. During the resting state scans, subjects were instructed to lay as still as possible, not think about anything in particular, and keep their eyes open and fixated on a yellow cross centered on a blue background. Additionally, a T_1-weighted anatomical scan was acquired for each subject and used as an anatomical underlay for the resting state fMRI results. Finally, coil sensitivity maps, coil noise measurements and a field map were collected for the image reconstruction of the MESMS and MESS data.

MR Data Acquisition

Imaging data were collected on a 3T GE MR750 system with a 32-channel receive head coil (Nova Medical). High-resolution T_1-weighted anatomical data were collected using a magnetization prepared 3D fast spoiled gradient echo (FSPGR) sequence (TI=600ms, TE=3.18ms, 8° flip angle, 1mm slice thickness, FOV=25cm, 256×256×172 matrix size).

Resting state data were collected with three echoes (TEs of 13.8ms, 32.5ms, and 51.2ms and a readout length of 17.5ms per echo), a 1.33-fold phase encode acceleration factor, 3.75x3.75x4mm resolution, and whole brain coverage (FOV=24cm, 64×64 matrix size, 36 sagittal slices). The slice coverage of 144mm was based on the average right-to-left width of the human brain, which is around 140mm, and was sufficient to acquire whole brain images for all our subjects. The MESMS data were acquired with a blipped-controlled aliasing in parallel imaging (blipped-CAIPI) EPI k-space trajectory (Setsompop et al., 2012). The

acquisition used a simultaneous multi-slice radiofrequency (SMS-RF) pulse with each pulse simultaneously exciting 3 sagittal slices, for a total of 12 separate excitations per TR. The SMS-RF pulse design utilized an optimized set of excitation phases to minimize peak RF (Wong, 2012). This optimization causes the 3 simultaneously excited slices to have a slice dependent phase. The MESS acquisition replicated this slice dependent phase in the respective single-slice RF pulses to match the MESMS acquisition as closely as possible. In addition, the MESS acquisition used the same blipped-CAIPI EPI trajectory as the MESMS acquisition. Other acquisition parameters for MESMS were: TR=0.87s, 690 volumes, and FA=56°. For MESS these parameters were: TR=2.61s, 230 volumes, and FA=80°. The flip angles were set at the Ernst angle assuming an average T_1 of 1.47s for water in gray matter (Ethofer et al., 2003).

The field map was acquired with the same resolution and slice locations as the resting state data. It was estimated from the phase difference of two echoes that were acquired with a gradient recalled acquisition in steady state (GRASS) sequence (TE1 = 6.5ms, TE2 = 8.5ms).

MR Image Reconstruction

To reconstruct the MESMS and MESS images, we used a quadratic penalized weighted least squares (QPWLS) SENSE reconstruction with a fast conjugate gradient Toeplitz-based iterative algorithm and a spatial roughness penalty (Fessler et al., 2005; Olafsson et al., 2006). The coil sensitivity maps, used in the SENSE reconstruction, were acquired using a blipped-CAIPI trajectory with no in-plane acceleration and a single slice excitation RF pulse with the same slice dependent phase differences as in the MESMS and MESS acquisitions. To estimate the coil sensitivity maps a single square-root-sum-of-squares image was formed from all the individual coil images and used to normalize each coil image. These coil images were reconstructed with an iterative field map corrected image reconstruction approach (Fessler et al., 2005). The field map correction was used to account for the echo spacing differences between the non-accelerated EPI coil sensitivity acquisition and the accelerated MESMS and MESS EPI acquisitions. Finally, the weights in the QPWLS SENSE reconstruction were generated from the coil noise correlation matrix (Pruessmann et al., 2001; Pruessmann et al., 1999). The correlation matrix was estimated by collecting data with no RF excitation and a blipped-CAIPI trajectory, followed by correlating the data from each coil, i.e., the coil noise samples, to data from all other coils.

MR data pre-processing

Data were processed using AFNI (Cox, 1996) and custom Python scripts (see meica.py provided with AFNI: http://afni.nimh.nih.gov/afni/). Each echo of the MESMS and MESS data was first corrected for slice timing. Next the functional data were motion corrected and registered to the anatomical data, using a transformation matrix constructed by concatenating the parameters of the rigid-body motion correction from the first echo time series with the parameters of the affine co-registration of the functional data to the T_1-weighted anatomical image. Optimally combined (OC) data were generated for both the MESMS and MESS data, by taking a weighted summation of the three echoes of the respective datasets, using the exponential weighting approach in (Posse et al., 1999).

Principal Component Analysis (PCA)

Prior to the ICA decomposition, the dimensionality of the data was estimated using multi-echo principal components analysis (ME-PCA) and a reduced dimensionality dataset was formed (Kundu et al., 2013; Kundu et al., 2014). For the ME-PCA approach, a PCA was first performed on the OC time series data. Then, each of the PCA component time series was fit on a per-voxel basis to the pre-processed time series from each of the three echoes, thus generating PCA weights (in units of signal change) for each echo. These voxel-wise weights were then separately fit to MR signal models for linear TE-dependence and TE-independence. F-statistics were computed for each model, where the magnitude of the F-statistic of the linear TE-dependence and TE-independence models indicated the degree of BOLD weighting and non-BOLD weighting, respectively, of the multi-echo weights for each component. Intensity weighted averages of the F-statistics were computed, with κ and ρ denoting the average intensity metrics for BOLD weighting and non-BOLD weighting, respectively. The κ and ρ metrics as well as the eigenvalues from the PCA were each separately sorted across components, and the elbows of the respective scree plots were determined. The elbow values were then used to determine threshold values for the κ and ρ metrics, and components with metrics that exceeded either threshold (indicating an above-threshold degree of BOLD or non-BOLD weighting) were used to construct a dimensionality reduced OC time series, while all other components were discarded. Details on the signal models, F-statistics, κ and ρ metrics, and determination of the thresholds are provided in the Appendix.

Independent Component Analysis (ICA)

Spatial ICA using the FastICA algorithm (Hyvarinen, 1999) with a *tanh* contrast function was applied to the dimensionality reduced OC time series data, producing a time-domain independent component mixing matrix (variance normalized). In the application of FastICA, whitening of the temporal covariance matrix was applied as a standard preprocessing step. In a manner similar to the fitting of the PCA components, independent component time series were fit using multiple least-squares regression on a per-voxel basis to the pre-processed time series from each of the three echoes, generating ICA weights for each echo. These weights were then fit to the linear TE-dependence and TE-independence models to generate F-statistics and component-level κ and ρ values that indicated BOLD and non-BOLD weighting, respectively. The κ and ρ metrics were then used to identify the BOLD-like components, according to the criteria described in the Appendix.

Generation and Comparison of Derived Datasets

To investigate the effects of temporal resolution, number of samples, temporal aliasing, and temporal bandwidth on the ability of ME-ICA to identify BOLD-related components, we generated several types of datasets that were derived from the MESMS data. Each of the derived datasets was analyzed with ME-PCA followed by ME-ICA.

First, we derived datasets from the MESMS data that were designed to match the characteristics of the MESS data. This was done by downsampling the MESMS data by a factor of 3, resulting in data with the same temporal sampling and number of volumes as the MESS data. The downsampling process generated three downsampled datasets (MESMS-

dsamp), with the first, second and third volumes used as starting volumes for each dataset. Note that these datasets inherited the dynamic features (e.g. motion and brain state) of the MESMS data while matching the temporal resolution and signal characteristics (i.e. temporal aliasing of high-frequency components) of the MESS data. This allowed for a more direct assessment of the effects of temporal resolution, without concerns for differences in brain dynamics that might have occurred between the MESMS and MESS runs.

Next, we generated datasets with the same temporal resolution as the MESMS-dsamp and MESS data, but with reduced temporal aliasing of high frequency components. For these the MESMS data were first filtered with a 37-tap finite impulse response (FIR) low-pass filter (LPF) with 0.19Hz cutoff frequency, and then downsampled by a factor of 3. This process yielded three sets of decimated data (MESMS-decimate) with the first, second and third volumes used as the starting volumes for each dataset. Comparison of the MESMS-dsamp and MESMS-decimate data enabled an assessment of the effect of temporal aliasing on the identification of BOLD-like components

We also generated two low-pass filtered MESMS datasets without downsampling. The first dataset used the LPF described earlier with a cutoff of 0.19Hz and the second dataset used a 35-tap FIR LPF with a cutoff of 0.38Hz. These filtered datasets were used to assess the effect of signal bandwidth on the identification of BOLD-like components. Finally, we applied interpolation to the MESS, MESMS-decimate, and MESMS-dsamp datasets to form derived datasets that had the same temporal resolution as the original MESMS dataset. These datasets allowed us to examine the effect of signal dimensionality on the ability to estimate BOLD dimensionality.

Paired t-tests (two-sided) were used to compare the number of BOLD-like components identified by ME-ICA for each pair of datasets (e.g. comparing the number of components between MESMS and MESS).

Results

As an example of the automated identification of non-BOLD components with ME-ICA, Figure 1 shows two non-BOLD independent components identified in the MESMS data. In the component maps shown in panel A, the spacing of the line artifacts in the axial views matches the spacing of the slices that were simultaneously excited in the MESMS acquisition. These types of structured artifacts have been noted in prior studies that have used simultaneous multi-slice excitations (Boubela et al., 2013; Kelley et al., 2013). Panel B shows an artifact component that is largely present in the sagittal sinus and most likely reflects vascular pulsations.

Figure 2 shows the number of BOLD-like principal components and independent components identified by ME-PCA and ME-ICA, respectively, for MESMS, MESS, and the various resampled and filtered versions of MESMS and MESS. For the data where multiple instances were calculated (based on the three phases of downsampling and decimation) we

also indicate the average number of accepted components across the three phases. Table 1 lists the number of accepted components averaged across subjects.

As shown in Fig. 2D, the number of BOLD-like independent components identified for MESMS was significantly ($t(11) = 5.48$; $p < 0.001$) greater than that for MESS. There was not a significant difference ($t(11)=1.78$, $p = 0.10$) between the number of accepted ICs for MESS and the average number (across phases) for MESMS-dsamp. This result indicates that a downsampled version of the MESMS data serves as a reasonable surrogate for the MESS data, and thus supports the use of different filtering and resampling options to explore the effects of temporal resolution and bandwidth on the ability to identify BOLD-like components.

The number of BOLD-like independent components identified for MESMS-decimate was significantly greater than the number of components for both MESS ($t(11) = 5.44$; $p < 0.001$) and MESMS-dsamp ($t(11) = 10.13$; $p < 0.001$), indicating that the reduction of high frequency signals prior to downsampling improves the ability to identify BOLD-like components. However, the number of BOLD-like components for MESMS-decimate was significantly lower ($t(11) = -2.56$, $p = 0.027$) than the number identified for MESMS, suggesting that either the inclusion of high frequency signals or the larger number of samples in the MESMS data contributes to the larger number of BOLD-like components.

To assess the role of high frequency signals in the ability to detect BOLD-like components, we examined the number of components in low-pass filtered versions of the MESMS data. As shown in Fig. 2E, the number of BOLD-like components identified when the MESMS data were low-pass filtered with a cut-off frequency of 0.19 Hz was significantly greater ($t(11) = 3.43$; $p = 0.006$) than the number identified in the MESMS data. When the cut-off frequency was increased to 0.38 Hz, the number of components identified in the low-pass filtered data was not significantly different ($t(11) = 1.70$, $p = 0.116$) than the number in the MESMS data. These findings indicate that the inclusion of high frequency signals does not enhance the identification of BOLD-like components. Instead, the results suggest that the presence of high-frequency noise components reduces the ability to detect BOLD-like components.

Next, we investigated whether increasing the number of samples through interpolation would improve the ability to detect the number of BOLD-like independent components. We found that interpolation significantly increased the number of identified components for the MESS ($t(11) = 4.77$; $p < 0.001$), MESMS-dsamp ($t(11) = 6.16$; $p < 0.001$), and MESMS-decimate ($t(11) = 3.74$; $p = 0.003$) datasets. As compared to MESMS, the interpolated versions of MESS and MESMS-dsamp had significantly ($t<-3.8$; $p<0.003$) smaller numbers of components, whereas the interpolated version of MESMS-decimate had a significantly larger ($t(11) = 2.94$; $p=0.0136$) number of BOLD-like components. The number of components for the low-pass filtered (0.19Hz) version of MESMS and the interpolated version of MESMS-decimate were not significantly different ($t(11) = 0.6425$; $p = 0.643$). This last result is expected as the two datasets have the same signal bandwidth and number of samples. Overall, our findings suggest that the identification of BOLD-like components

benefits from both the removal of high-frequency noise components and an increase in the dimensionality of the signal space.

Figures 3 and 4 provide a qualitative view of how the higher temporal resolution of MESMS can lead to the automated identification of a greater number of BOLD-like independent components. Panels 3A and 3D show examples of two BOLD-like independent components (4 slices from each component) that were consistently identified in each of the three phases of the MESMS-dsamp data, where each row in a panel represents the component map from one of the phases. Note that there is great consistency in the component maps across the three phases. In the bottom two rows, we show two component maps that were identified in the MESMS data that showed a strong spatial similarity to the MESMS-dsamp component maps. In the component maps on the lefthand side of Figure 3, the left and right visual cortex regions in the MESMS-dsamp component (Panel 3A) are split into the two MESMS components shown in panels 3B and 3C. The corresponding component time courses are shown in Figure 4A, with the MESMS time courses indicated by the blue and green solid lines and the MESMS-dsamp time courses from the different phases indicated by the dashed lines. The MESMS-dsamp time courses are seen to follow excursions in both MESMS component 1 (blue arrows) and MESMS component 2 (green arrows), providing evidence for dynamic splitting of the MESMS-dsamp component. In the component maps on the righthand side of Figure 3, the MESMS-dsamp component (Panel D) is split into anterior and posterior MESMS components, shown in panels E and F, respectively. The corresponding component time courses are shown in Figure 4B, with evidence of dynamic splitting (green and blue arrows) of the MESMS-dsamp component into the two MESMS components.

Discussion

We have examined in detail the effect of temporal resolution and signal bandwidth on the ability of ME-ICA to identify BOLD-like independent components. We found that the greater temporal resolution and bandwidth achieved with a MESMS acquisition led to the identification of a significantly greater number of BOLD-like components as compared to MESS. The number of components identified with MESS was comparable to that obtained with downsampled versions of the MESMS data (with equivalent temporal resolution), providing support for the subsequent application of various resampling and filtering operations to better understand the factors affecting the performance of the ME-ICA approach.

We used different filtering options to investigate the effect of signal bandwidth on performance. We found that the application of low-pass filtering prior to downsampling (to generate MESMS-decimate) yielded a greater number of BOLD-like components as compared to MESMS-dsamp, indicating that the reduced ability of ME-ICA to identify BOLD-like components in the MESMS-dsamp data was primarily due to temporal aliasing of noise sources. Furthermore, low-pass filtered versions of the MESMS data (without downsampling) yielded either a significantly greater or comparable number of identified components as the original MESMS data, providing further evidence that the removal of high-frequency components benefits the performance of ME-ICA. Note that the number of

time points in the low-pass filtered versions was the same as that for the original MESMS data. This finding suggests that low-pass filtering of high temporal resolution datasets is of general benefit to the ME-ICA approach. As discussed in further detail below, this result suggests that the increase in performance due to the attenuation of high-frequency physiological artifacts and thermal noise outweighs the loss of information regarding high frequency functional signals. In other words, when considering the advantages of the higher temporal resolution, the ability to minimize temporal aliasing of high frequency noise components (so that they can be efficiently removed prior to further analysis) appears to be more important than capturing the high frequency content of functional signals.

We used interpolation to directly examine the effect of nominal temporal resolution on performance, and found that increasing the number of temporal samples led to a greater number of identified BOLD-like components. As interpolation does not add any new information to the time series data, these results suggest that the ME-ICA process can more effectively find BOLD-like components when the dimensionality of the signal space is increased. Overall, our findings suggest that ME-ICA performance is optimized when both the dimensionality of the signal space is maximized and high-frequency components are reduced. Note that these findings also suggest that interpolation of low-temporal resolution datasets may be useful as a general approach for improving ME-ICA performance with respect to data dimensionality in the ICA decomposition. However, the possible increase in the number of accepted components for an interpolated low-temporal resolution acquisition will still be lower than that of data acquired with higher temporal resolution. This can be seen in the bottom row of Figure 2, where the MESMS data has a significantly higher number of accepted IC’s as compared to the interpolated MESS data.

For the comparison of different acquisitions and processing options, we used the number of BOLD-like independent components as a metric of performance. In prior work, this metric has also been referred to as the BOLD degrees of freedom (DOF) and used to assess the complexity of global functional activity across conditions, such as varying levels of anesthesia (Kundu et al., 2013; Kundu et al., 2014). It has also been used to assess the overall BOLD sensitivity of various pulse sequences (Kundu et al., 2014). An increase in BOLD DOF is also beneficial when using independent component regression (ME-ICR) to assess functional connectivity in ICA space (Kundu et al., 2013; Kundu et al., 2014). The findings of the current study demonstrate the sensitivity of this metric to variations in both the acquisition and processing of the data. This suggests that care must be taken to ensure uniformity in the acquisition and processing of data across experiments that use DOF as a measure of functional complexity.

The finding that increased signal dimensionality and decreased high-frequency noise leads to more fragmentation of network components into regional representations and concurrently more effective degrees of freedom in denoised time series may extend beyond the context of ME-ICA. While spatial upsampling and interpolation is a common preprocessing step, temporal upsampling may aid in decomposition analyses of conventional fMRI towards higher-dimensional and thus more fine-grained analyses. In cases of automatic dimensionality estimation for ICA, such as probabilistic PCA (Tipping and Bishop, 1999), temporal upsampling may offer a measure of dynamical control over

dimensionality. As for the reason why increasing nominal data dimensionality leads to an increase in effective dimensionality, one possibility is that optimizing the kurtosis contrast between ICA components (Hyvarinen, 1999) is similar to optimizing under a sparsity penalty (Daubechies et al., 2009). The compressive sensing aspect of ICA is thus invoked and an inherent sensitivity to data dimensionality is suggested. In light of these findings, further study of ICA dimensionality in fMRI decomposition is warranted, especially since ICA is a key tool in ongoing and future fMRI studies, with advanced acquisition initiatives focusing heavily on increasing acquisition resolution. In addition, a study involving a progressive increase in upsampling factor followed by a count of the number of BOLD (in the case of ME-ICA) or otherwise network-like components may provide further insight into the intrinsic dimensionality of fMRI datasets.

With the increasing availability of fast imaging acquisition methods, such as the simultaneous multi-slice approach used in this study, there has been growing interest in the characterization of resting-state brain activity with high temporal resolution. A number of recent studies have used high temporal resolution acquisitions (with TRs ranging from 100ms to 647ms) to characterize resting-networks at frequencies above the standard 0.1 Hz cutoff frequency that has been used in prior studies (Boubela et al., 2013; Gohel and Biswal, 2014; Kalcher et al., 2014; Lee et al., 2013). The networks found at the higher frequency bands tend to mirror those found in the lower frequency bands, but with an overall decrease in sensitivity, reflecting the power-law type decrease in spectral energy that has been observed for resting-state fMRI fluctuations (He, 2011). (Chen and Glover, 2014) reported that the amplitude of resting-state fMRI signal correlations showed a linear dependence on echo-time for frequencies ranging from 0.01 up to 0.5 Hz, suggesting the presence of BOLD-like components across a broad range of frequencies. However, the dependence was much weaker at the higher frequencies, falling off steeply for frequencies above 0.1 Hz. Despite the decreased sensitivity observed at higher frequencies, the characterization of higher frequency networks may prove to be useful for studying the dynamics of time-varying connectivity, as the correlations at high frequencies can stabilize more quickly within a specified time window as compared to those computed at lower frequencies (Lee et al., 2013).

One clear advantage of high temporal resolution acquisitions is the improved ability to isolate high frequency physiological noise components, such as signals related to cardiac and respiratory activity, that are typically temporally aliased with standard acquisitions (Lee et al., 2013). (Kalcher et al., 2014) have shown that maps of low-frequency connectivity (< 0.1 Hz) in the basal ganglia show a greater level of sensitivity when acquired with a high temporal resolution (TR = 354 ms) acquisition as compared to a standard acquisition (with TR = 1800 ms) and attributed the improved performance to the ability to filter out high frequency physiological fluctuations. These findings are consistent with those of the current study, in which low-pass filtering increased the ability to identify BOLD-like components. For the ME-ICA approach, it appears that the gains achieved by filtering out high frequency artifacts and thermal noise components outweigh the loss of high frequency BOLD-like signal components (which have significantly less power than the low-frequency BOLD-like components). Thus, the performance gain for MESMS combined with ME-ICA reflects the overall ability of the MESMS approach to minimize temporal aliasing of high-frequency

nuisance signals, as opposed to any specific tuning of the ME-ICA algorithm to better detect low-frequency components.

Our findings are generally consistent with those that have been reported in preliminary studies comparing MESMS and MESS acquisitions. (Boyacioglu et al., 2013) found evidence that MESMS provides a stronger representation in frontal inferior regions of an independent component containing the default mode network. In a follow-up study, the same group (Boyacioglu et al., 2014) reported that after the manual detection and removal of non-BOLD noise components, MESMS identified 10 to 12 additional resting-state networks as compared to MESS, and hypothesized that the improvement was due to the improved ability of MESMS to separate physiological noise sources into individual components. In a preliminary study comparing MESMS with downsampled versions of the same data, we found that functional connectivity maps in subcortical regions were more clearly delineated with ME-ICA when using the MESMS data (Olafsson et al., 2013). A preliminary version of the present study showing a greater number of BOLD-like components with MESMS was presented in (Olafsson et al., 2014).

In fMRI, it is well established that the BOLD signal usually has an accompanying inflow effect and that these inflow effects are accentuated as the repetition time of the acquisition decreases. The ME-ICA algorithm will tend to retain components where changes in neural activity give rise to both significant BOLD and inflow effects, but could reject components for which there is a high inflow effect and minimal BOLD effect. Although the majority of functional components are likely to exhibit both BOLD and in-flow effects, it is possible that there are also inflow components that reflect functional activity primarily localized to the arterial side where BOLD effects would be limited due to the low concentration of deoxyhemoglobin. Further work to characterize the ability of ME-ICA to identify such components would be of interest.

In the present study, sagittal acquisitions with whole-brain coverage were employed with slice-acceleration in the left-right direction and in-plane acceleration in the anterior-posterior direction. The choice of this orientation was based on preliminary studies indicating that the acceleration performance of the multi-channel receive coil was better in the anterior-posterior and left-right directions as compared to the superior-inferior axis. However, given the dependence of acceleration performance on coil geometry, the optimal choice of orientation will depend on the specific coil used. As the primary gains of MESMS stem from the ability to remove high temporal frequency noise sources, it is likely that these gains will also apply to acquisitions with other slice orientations, such as axial and coronal. Nevertheless, a follow-up study similar in scope to the present study would be useful to confirm this expectation.

In this study, we used the increased acquisition efficiency afforded by the simultaneous multi-slice method to increase the temporal resolution for multi-echo acquisitions while maintaining a fairly conventional standard spatial resolution, yielding a protocol with 3-echoes acquired with a temporal resolution of 870ms and 3.75×3.75×4mm spatial resolution. It is also possible to leverage the simultaneous multi-slice method to achieve increases in both temporal and spatial resolution. For example, the Human Connectome Project (HCP)

protocol uses simultaneous multi-slice method to acquire single-echo whole-brain data with a temporal resolution of 720 ms with 2 mm isotropic spatial resolution (Smith et al., 2013). As part of the HCP pre-processing pipeline, these data are automatically denoised using spatial ICA combined with a multi-level classifier that uses spatial and temporal features to distinguish “signal” components from “noise” components (Griffanti et al., 2014; Salimi-Khorshidi et al., 2014). It has been shown that this denoising process (known as FMRIB’s ICA-based X-noiseifier (FIX)) benefits from the higher temporal resolution afforded by the simultaneous multi-slice acquisition (Griffanti et al., 2014). One potential limitation of the FIX approach is the need for a training set to design and optimize the classifier. This requirement may be difficult to meet for studies with small sample sizes and unique acquisition protocols. In contrast, the ME-ICA approach can denoise datasets without an explicit need for training of a classifier. Further studies focused on a systematic comparison of the FIX and ME-ICA approaches would be useful.

Acknowledgements

The authors would like to thank Jia Guo, Kun Lu, Eman Ghobrial, Vinai Roopchansingh, Wen-Ming Luh, and Noah Brenowitz for helping with setting up the MESMS acquisition pipeline, Chi Wah Wong on discussions for the resting state experimental setup, and Souheil Inati for discussions on ME-ICA and MESMS implementations. This work was supported in part by NIH Grants R01NS051661 and R21MH096495, and ONR MURI Award No. N00014-10-1-0072.

Appendix

In this appendix, we summarize the signal models and algorithms that have been previously presented in prior work (Kundu et al., 2013; Kundu et al., 2012; Kundu et al., 2014) and provide additional explanation of the approach. For the specific implementation details, the reader is referred to the Python scripts that are available as meica.py through http://afni.nimh.nih.gov/afni/.

The signal models for TE-dependence (BOLD weighting measure) and TE-independence (non-BOLD weighting measure) are:

$$\Delta S_{TE}/S_{TE} = -\Delta R_2^* TE$$

$$\Delta S_{TE}/S_{TE} = \Delta S_0/S_0$$

where ΔS_{TE} is the signal change from mean for a fluctuation at a specified TE (i.e. its PCA or ICA weight from the least squares fit of the OC time series), and S_{TE} is the signal mean at the same TE, ΔR_2* is the change in susceptibility-weighted transverse relaxation time that is solved for in the TE-dependence BOLD model, S_0 is the initial signal intensity, and ΔS_0 is the change in initial signal intensity that is solved for in the TE-independence non-BOLD model.

Goodness of fit metrics for the MR signal models were computed at each voxel with the following formulas for the respective F-statistics (written in extra sum of squares form):

$$F_{R_2^*} = \frac{\frac{\alpha_0 - \alpha_{R_2^*}}{\alpha_{R_2^*}}}{\frac{df_0 - df_{R_2^*}}{df_{R_2^*}}}$$

$$F_{S_0} = \frac{\frac{\alpha_0 - \alpha_{S_0}}{\alpha_{S_0}}}{\frac{df_0 - df_{S_0}}{df_{S_0}}}$$

where α_0 is the null variance (equal to the sum of the squares across echoes of the per echo PCA or ICA weights), $\alpha_{R_2^*}$ is the residual variance between the per echo PCA or ICA weights and the model fit to the TE-dependence model, α_{S_0} is the residual variance from the fit to the TE-independence model, df_0 is the total number of degrees of freedom for the signal models (equal to the number of echoes, 3), and $df_{R_2^*}$ and df_{S_0} are the degrees of freedom used in the respective fits (1 each).

The κ and ρ metrics are defined for each component as the weighted sum of the F-statistics across voxels:

$$\kappa_c = \frac{\Sigma_v^V Z_{c,v}^p F_{c,v,R_2^*}}{\Sigma_v^V Z_{c,v}^p}$$

$$\rho_c = \frac{\Sigma_v^V Z_{c,v}^p F_{c,v,S_0}}{\Sigma_v^V Z_{c,v}^p}$$

where *c* is the component index, *v* is the voxel index, V is the total number of voxels, $Z_{c,v}$ is a spatially normalized signal amplitude that characterizes the relative contribution of the *c*th component to the signal from the *v*th voxel, and *p* is a power factor (default 2)

The κ and ρ thresholds for estimating data dimensionality in ME-PCA are based on the elbows κ_{elbow} and ρ_{elbow} of the κ and ρ scree plots, respectively and tuning factors κ_{DAW} and ρ_{DAW} as follows:

$$\kappa_{thr} = \frac{\boldsymbol{\kappa_{ref}} \cdot \boldsymbol{W}_\kappa}{\Sigma \boldsymbol{W}_\kappa}$$

$$\rho_{thr} = \frac{\boldsymbol{\rho_{ref}} \cdot \boldsymbol{W}_\rho}{\Sigma \boldsymbol{W}_\rho}$$

where $\boldsymbol{\kappa_{ref}}$ is the 3-element vector [κ_{elbow}, $F(1,N_{echo}-1)_{p<0.05}$, $F(1,N_{echo}-1)_{p<0.025}$], sorted in ascending order and $\boldsymbol{W}_{\kappa}$ is the vector [κ_{DAW},1,1] with $\kappa_{DAW} \geq 1$. Similarly, $\boldsymbol{\rho_{ref}}$ is the vector [ρ_{elbow}, $F(1,N_{echo}-1)_{p<0.05}$, $F(1,N_{echo}-1)_{p<0.025}$], sorted in ascending order and $\boldsymbol{W}_{\rho}$ is the vector [ρ_{DAW},1,1] with $\rho_{DAW} \geq 1$. Increasing the parameters κ_{DAW} and ρ_{DAW} weights the respective thresholds κ_{thr} and ρ_{thr} towards the lowest F value, thus increasing the number of principal components kept in the dimensionality-reduced data in a way that makes BOLD and non-BOLD signal contributions specifically tunable. This approach is dynamic by adjusting κ_{thr} and ρ_{thr} around the intrinsic characteristics as represented by κ_{elbow} and ρ_{elbow} and stable through the use of reference values for F at nominal significance values. In this study κ_{DAW} and ρ_{DAW} were set to 10 and 1, respectively, which increased the relative sensitivity to BOLD signals in the dimensionality reduction process.

In the ME-ICA, independent components were classified into BOLD vs. non-BOLD categories according to an “accept all, reject some” policy. Thus, from the full set of components, non-BOLD components were first identified for rejection using the following criteria:

(a) $\kappa < \rho$, i.e. the average intensity metric for non-BOLD weighting is greater than the corresponding metric for BOLD-weighting.

(b) The number of significant S_0-weighted voxels was greater than the number of significant R_2*-weighted voxels, where significance was assessed with the F-statistic at the $p<0.05$ significance level.

(c) There was a greater overlap of the rank-thresholded signal change maps (i.e. ICA weights) with the thresholded ($p < 0.05$)F_{S_0} maps than with the thresholded $F_{R_2^*}$ maps, where the overlap was computed as the Dice metric. For the rank-thresholding of the signal change maps, the N voxels with the highest amplitude were retained, where N denotes the number of voxels in either the thresholded F_{S_0} or $F_{R_2^*}$ maps.

(d) There was a greater $F_{R_2^*}$ magnitude in unclustered voxels (i.e. spatial noise) in rank-thresholded signal change maps versus clustered voxels, based on a two-sample t-test. This criterion utilizes spatial noise to sample an empirically-derived null distribution for $F_{R_2^*}$, asserting that the magnitude of $F_{R_2^*}$ in clustered voxels indicates functional neuroanatomy if significantly higher than the empirical null $F_{R_2^*}$.

A further refinement was made to identify BOLD-like artifacts that are characteristic of fluctuations in the draining veins. These fluctuations exhibit high variance and mid-range κ values. In addition, the refinement identifies low variance (i.e. “empty”) components. After ranking the above metrics (κ, ρ, Dice metrics for $F_{R_2^*}$ and F_{S_0} map overlap with the signal change maps, t-statistics representing $F_{R_2^*}$ magnitude in clustered voxels vs. unclustered voxels, and counts of voxels with $F_{R_2^*}$ weighting vs. those with F_{S_0} weighting) in ascending

order towards greater artifact weighting or lesser BOLD weighting, the ranks of the different metrics v_i over the T=7 tests were summed to form the rank-sum

$$\gamma_{NB}=\sum_{i}^{T} rank\,(v_i)$$

for each component, such that larger values of γ_{NB} corresponded to components that exhibited a greater degree of non-BOLD-like characteristics. A critical value ($\gamma_{critical}$) was determined using $rank(\kappa_{elbow})$ as an initial guess for the true number of functional BOLD components in the dataset.

$$\gamma_{critical}=rank\,(\kappa_{elbow}) \times T$$

High rank-sum ($\gamma_{NB} > \gamma_{critical}$) components explaining percentages of variance exceeding that of the 75th percentile of the top κ-ranked (i.e. $\kappa > \rho$) independent components were classified as “mid-κ” artifacts, while high rank-sum components explaining percentages of variance below the 25th percentile of the top κ-ranked independent components were classified as “empty” and ignored (i.e. not considered as part of the BOLD component set, but not projected out in time series denoising). The remaining components were classified as BOLD-like components. This approach identifies BOLD-like but non-functional components that are close to failure on several tests or fail distinctly in a small number of tests. More metrics indicative of TE-dependence or functional likeness can also be accommodated, without requirements for the distribution of any particular test statistic.

References

Boubela RN, Kalcher K, Huf W, Kronnerwetter C, Filzmoser P, Moser E. Beyond Noise: Using Temporal ICA to Extract Meaningful Information from High-Frequency fMRI Signal Fluctuations during Rest. Front Hum Neurosci. 2013; 7:168. [PubMed: 23641208]

Boyacioglu, R.; Bersch, J.; Poser, BA.; Koopmans, P.; Barth, M.; Norris, DG. Short TR resting state data acquired with a simultaneous multislice multi-echo sequence at 7T, comparison with multi-echo; 21st Annual Scientific Meeting of the International Society for Magnetic Resonance in Medicine; Salt Lake City, Utah. 2013; p. 3707

Boyacioglu, R.; Schulz, J.; Koopmans, P.; Barth, M.; Norris, DG. Improving sensitivity and specificity for RS fMRI using multiband multi-echo EPI at 7T; 22nd Annual Scientific Meeting of the International Society for Magnetic Resonance in Medicine; Milan, Italy. 2014; p. 1502

Chen, J.; Glover, GH. Reduced BOLD fractional Contributions to Resting-state(RS) Functional Connectivity(FC) above 0.1 Hz; 20th Annual Meeting of the Organization for Human Brain Mapping; Hamburg, Germany. 2014; p. 1585

Cox RW. AFNI: software for analysis and visualization of functional magnetic resonance neuroimages. Comput Biomed Res. 1996; 29:162–173. [PubMed: 8812068]

Daubechies I, Roussos E, Takerkart S, Benharrosh M, Golden C, D’Ardenne K, Richter W, Cohen JD, Haxby J. Independent component analysis for brain fMRI does not select for independence. Proc Natl Acad Sci U S A. 2009; 106:10415–10422. [PubMed: 19556548]

Ethofer T, Mader I, Seeger U, Helms G, Erb M, Grodd W, Ludolph A, Klose U. Comparison of longitudinal metabolite relaxation times in different regions of the human brain at 1.5 and 3 Tesla. Magn Reson Med. 2003; 50:1296–1301. [PubMed: 14648578]

Feinberg DA, Moeller S, Smith SM, Auerbach E, Ramanna S, Gunther M, Glasser MF, Miller KL, Ugurbil K, Yacoub E. Multiplexed echo planar imaging for sub-second whole brain FMRI and fast diffusion imaging. PLoS One. 2010; 5:e15710. [PubMed: 21187930]

Fessler JA, Lee S, Olafsson VT, Shi HR, Noll DC. Toeplitz-based iterative image reconstruction for MRI with correction for magnetic field inhomogeneity. IEEE Transactions on Signal Processing. 2005; 53:3393–3402.

Gohel SR, Biswal BB. Functional Integration Between Brain Regions at Rest Occurs in Multiple-Frequency Bands. Brain Connect. 2015; 5:23–34. [PubMed: 24702246]

Griffanti L, Salimi-Khorshidi G, Beckmann CF, Auerbach EJ, Douaud G, Sexton CE, Zsoldos E, Ebmeier KP, Filippini N, Mackay CE, Moeller S, Xu J, Yacoub E, Baselli G, Ugurbil K, Miller KL, Smith SM. ICA-based artefact removal and accelerated fMRI acquisition for improved resting state network imaging. Neuroimage. 2014; 95:232–247. [PubMed: 24657355]

He BJ. Scale-free properties of the functional magnetic resonance imaging signal during rest and task. Journal of Neuroscience. 2011; 31:13786–13795. [PubMed: 21957241]

Hyvarinen A. Fast and robust fixed-point algorithms for independent component analysis. IEEE Trans Neural Netw. 1999; 10:626–634. [PubMed: 18252563]

Kalcher K, Boubela RN, Huf W, Bartova L, Kronnerwetter C, Derntl B, Pezawas L, Filzmoser P, Nasel C, Moser E. The spectral diversity of resting-state fluctuations in the human brain. PLoS One. 2014; 9:e93375. [PubMed: 24728207]

Kelley, ME.; Duff, EP.; Bijsterbosch, JD.; Voets, NL.; Filippini, N.; Moeller, S.; Xu, J.; Yacoub, ES.; Auerbach, EJ.; Ugurbil, K.; Smith, SM.; Miller, KL. An assessment of motion artefacts in multi band EPI for high spatial and temporal resolution resting state FMRI; 21st Annual Scientific Meeting of the International Society for Magnetic Resonance in Medicine; Salt Lake City, Utah. 2013; p. 3275

Kundu P, Brenowitz ND, Voon V, Worbe Y, Vertes PE, Inati SJ, Saad ZS, Bandettini PA, Bullmore ET. Integrated strategy for improving functional connectivity mapping using multiecho fMRI. Proc Natl Acad Sci U S A. 2013; 110:16187–16192. [PubMed: 24038744]

Kundu P, Inati SJ, Evans JW, Luh WM, Bandettini PA. Differentiating BOLD and non-BOLD signals in fMRI time series using multi-echo EPI. Neuroimage. 2012; 60:1759–1770. [PubMed: 22209809]

Kundu P, Santin MD, Bandettini PA, Bullmore ET, Petiet A. Differentiating BOLD and non-BOLD signals in fMRI time series from anesthetized rats using multi-echo EPI at 11.7T. Neuroimage. 2014; 102P2:861–874. [PubMed: 25064668]

Lee HL, Zahneisen B, Hugger T, LeVan P, Hennig J. Tracking dynamic resting-state networks at higher frequencies using MR-encephalography. Neuroimage. 2013; 65:216–222. [PubMed: 23069810]

Moeller S, Yacoub E, Olman CA, Auerbach E, Strupp J, Harel N, Ugurbil K. Multiband multislice GE-EPI at 7 tesla, with 16-fold acceleration using partial parallel imaging with application to high spatial and temporal whole-brain fMRI. Magn Reson Med. 2010; 63:1144–1153. [PubMed: 20432285]

Olafsson, V.; Guo, J.; Wong, CW.; Kundu, P.; Inati, S.; Luh, W-M.; Roopchansingh, V.; Brenowitz, N.; Bandettini, P.; Wong, E.; Liu, T. High spatial and temporal resolution fcMRI with BOLD selectivity using multiecho simultaneous multislice EPI; Proceedings of the 20th ISMRM; Melbourne. 2012; p. 2068

Olafsson, V.; Kundu, P.; Wong, CW.; Guo, J.; Bandettini, P.; Wong, E.; Liu, T. Improved detection of subcortical resting state networks in functional MRI using multi-echo simultaneous multi-slice acquisition; Proceedings of the 21th ISMRM; Salt Lake City. 2013; p. 3318

Olafsson, V.; Kundu, P.; Wong, CW.; Guo, J.; Lu, K.; Ghobrial, E.; Bandettini, P.; Wong, EC.; Liu, TT. Improved Detection of BOLD-like Independent Components with Multi-Echo Simultaneous Multi-Slice Acquisitions and Multi-echo ICA; 22nd Annual Scientific Meeting of the International Society for Magnetic Resonance in Medicine; Milan, Italy. 2014; p. 4139

Olafsson, V.; Lee, S.; Fessler, JA.; Noll, DC. Fast Toeplitz Based Iterative SENSE Reconstruction; Proceedings of the 14th ISMRM; Seattle. 2006; p. 2459

Posse S, Wiese S, Gembris D, Mathiak K, Kessler C, Grosse-Ruyken ML, Elghahwagi B, Richards T, Dager SR, Kiselev VG. Enhancement of BOLD-contrast sensitivity by single-shot multi-echo functional MR imaging. Magn Reson Med. 1999; 42:87–97. [PubMed: 10398954]

Pruessmann KP, Weiger M, Bornert P, Boesiger P. Advances in sensitivity encoding with arbitrary k-space trajectories. Magn Reson Med. 2001; 46:638–651. [PubMed: 11590639]

Pruessmann KP, Weiger M, Scheidegger MB, Boesiger P. SENSE: sensitivity encoding for fast MRI. Magn Reson Med. 1999; 42:952–962. [PubMed: 10542355]

Salimi-Khorshidi G, Douaud G, Beckmann CF, Glasser MF, Griffanti L, Smith SM. Automatic denoising of functional MRI data: combining independent component analysis and hierarchical fusion of classifiers. Neuroimage. 2014; 90:449–468. [PubMed: 24389422]

Setsompop K, Gagoski BA, Polimeni JR, Witzel T, Wedeen VJ, Wald LL. Blipped-controlled aliasing in parallel imaging for simultaneous multislice echo planar imaging with reduced g-factor penalty. Magn Reson Med. 2012; 67:1210–1224. [PubMed: 21858868]

Smith SM, Beckmann CF, Andersson J, Auerbach EJ, Bijsterbosch J, Douaud G, Duff E, Feinberg DA, Griffanti L, Harms MP, Kelly M, Laumann T, Miller KL, Moeller S, Petersen S, Power J, Salimi-Khorshidi G, Snyder AZ, Vu AT, Woolrich MW, Xu J, Yacoub E, Ugurbil K, Van Essen DC, Glasser MF, Consortium WU-MH. Resting-state fMRI in the Human Connectome Project. Neuroimage. 2013; 80:144–168. [PubMed: 23702415]

Tipping ME, Bishop CM. Probabilistic principal component analysis. Journal of the Royal Statistical Society Series B-Statistical Methodology. 1999; 61:611–622.

Wong, E. Optimized phase schedules for minimizing peak RF power in simultaneous multi-slice RF excitation pulses; Proceedings of the 20th Annual Meeting of ISMRM; Melbourne, Australia. 2012; p. 2209

Research Highlights for

Enhanced Identification of BOLD-like Components with Multi-Echo Simultaneous Multi-Slice (MESMS) fMRI and Multi-Echo ICA

- Analyzed multi-echo simultaneous multi-slice (MESMS) fMRI data with ME-ICA
- ME-ICA used to assess the gains of MESMS over multi-echo single-slice (MESS) fMRI
- MESMS fMRI natively yields more BOLD components than MESS fMRI
- Gains due to decreased aliasing and increased signal dimensionality of MESMS fMRI
- ME-ICA automatically identifies SMS artificats in MESMS fMRI data

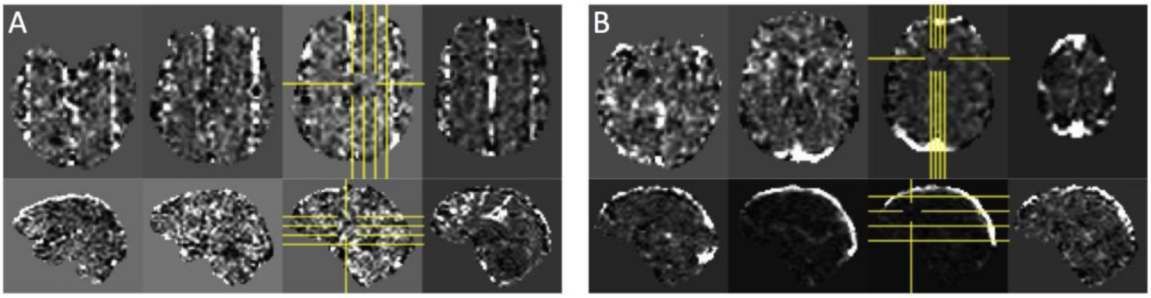

Figure 1.

Two non-BOLD independent components identified in the MESMS data. (A) In this component map the spacing of the line artifacts in the axial views matches the spacing of the slices that were simultaneously excited in the MESMS acquisition. (B) In this component most of the energy is located in the sagittal sinus, most likely reflecting vascular pulsations.

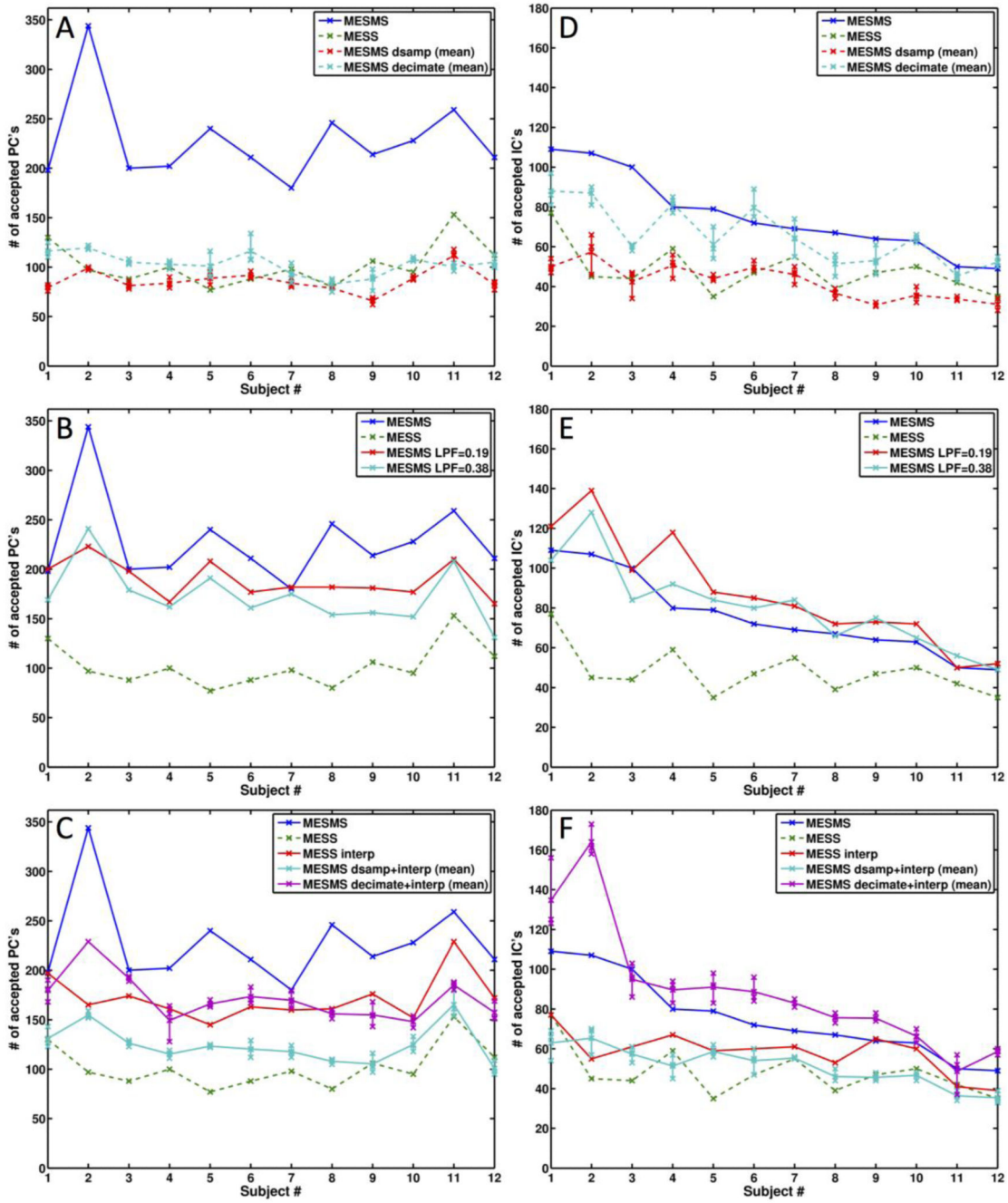

Figure 2.

Plots showing the number of BOLD-like PC's (left column) and IC's (right column) identified using ME-PCA and ME-ICA, respectively. The number of components is shown for each subject, with the subjects ordered by the number of BOLD-like ICs in the MESMS data. The solid and dashed lines indicate data that have 690 and 230 volumes, respectively. For data that were downsampled (MESMS dsamp, MESMS decimate, MESMS dsamp +interp, MESMS decimate+interp), the numbers of components from the 3 phases are shown by the symbols along the vertical lines and the mean number is indicated by the

connecting curve. The numbers of components for MESMS and MESS are shown in all plots for reference. Top row: Number of components for MESMS and datasets with lower temporal resolution (MESS, MESMS dsamp, and MESMS decimate). Middle row: Comparison of original MESMS data with versions that have been low-pass filtered with cutoff frequencies of 0.19Hz and 0.38Hz. Bottom row: MESMS compared with interpolated versions of the MESS, MESMS dsamp, and MESMS decimate datasets.

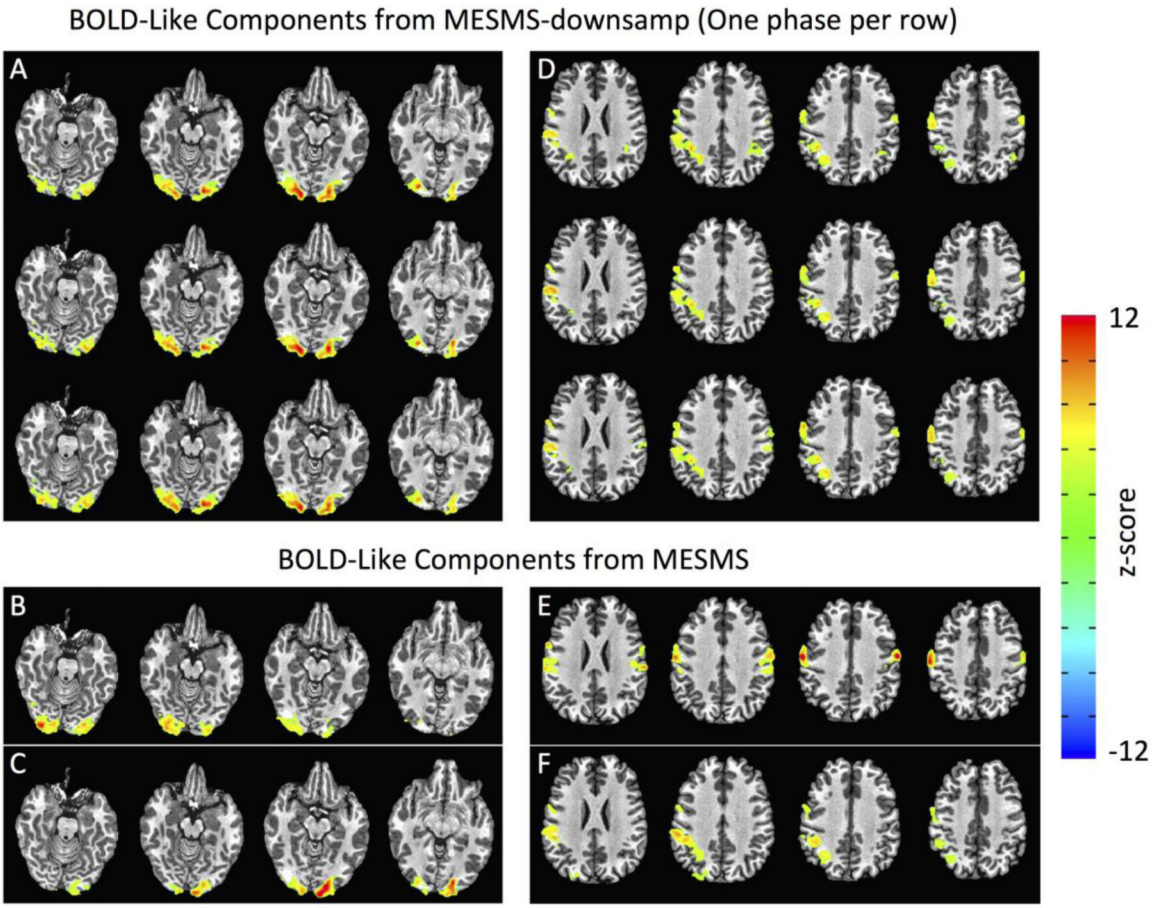

Figure 3.

Example of component splitting identified with MESMS. (A,D) Maps of two BOLD-like independent components (4 slices from each component). Each row in a panel represents the component map from one of the three phases of the MESMS-dsamp data. (B,C) Component maps identified in the MESMS data, with the visual cortex component seen in the MESMS-dsamp data (panel A) split into left and right regions. (E,F) Component maps identified in the MESMS data, with the component from the MESMS-dsamp data (panel D) split into anterior and posterior MESMS components.

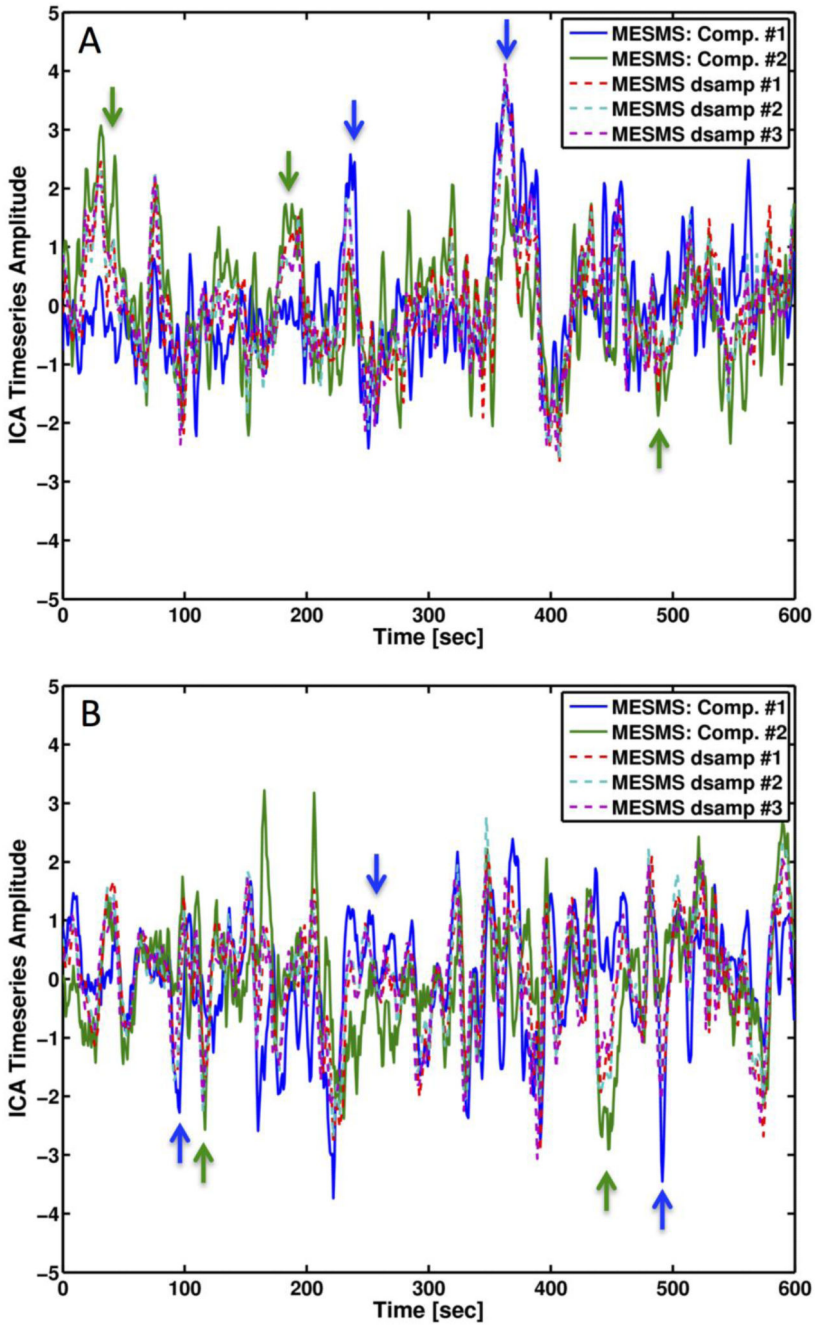

Figure 4.

Time courses for the independent components shown in Figure 3. (A) Time courses for MESMS-dsamp (dashed lines) and MESMS components (solid lines), corresponding to the maps shown in Figure 3A-C. (B) Time courses for MESMS-dsamp (dashed lines) and MESMS components (solid lines), corresponding to the maps shown in Figure 3D-F. For both panels, the arrows indicate times where the MESMS-dsamp component follows either MESMS component #1 (blue) or component #2 (green).

Table 1

Number of BOLD-like principal components (PCs) and independent components (ICs) averaged across subjects for different versions of the data. For versions with multiple phases, the overall average across subjects and phases is shown and the average values (across subjects) for each of the 3 phases are listed in the parentheses.

	MESMS	**MESS**	**MESMS dsamp (mean)**	**MESMS decimate (mean)**	**MESMS LPF=0.19**	**MESMS LPF=0.38**	**MESS interp**	**MESMS dsamp+interp (mean)**	**MESMS decimate+interp (mean)**
PCs	228	102	86 (86,87,86)	103 (103,103,103)	189	173	171	124 (127,122,124)	172 (171,173,172)
ICs	76	48	42 (42,41,44)	66 (65,65,67)	88	81	58	51 (50,52,53)	89 (85,92,91)